A magnetic assembly approach to chiral superstructures

Authors: Zhiwei Li§, Qingsong Fan, Zuyang Ye, Chaolumen Wu, Zhongxiang Wang, Yadong Yin*

5 **Affiliations:**

10

15

20

Department of Chemistry, University of California, Riverside, CA 92521, USA.

*Corresponding author. Email: yadong.yin@ucr.edu.

§Present address: Department of Chemistry and International Institute for Nanotechnology, Northwestern University, Evanston, Illinois 60208, United States

Abstract: Colloidal assembly into chiral superstructures usually is accomplished with templating or lithographic patterning methods that are only applicable to materials with specific compositions and morphologies over narrow size ranges. Here, chiral superstructures can be rapidly formed by magnetically assembling materials of any chemical compositions at all scales, from molecules to nano- and microstructures. We show that a quadrupole field chirality is generated by permanent magnets caused by consistent field rotation in space. Applying the chiral field to magnetic nanoparticles produces long-range chiral superstructures controlled by field strength at the samples and orientation of the magnets. Transferring the chirality to any achiral molecules is enabled by incorporating guest molecules, such as metals, polymers, oxides, semiconductors, dyes, and fluorophores, into the magnetic nanostructures.

One-Sentence Summary: A quadrupole field chirality in permanent magnets to assemble any achiral materials into chiral superstructures.

Superstructures of colloidal particles can assemble with chiral symmetry (1-5). The driving force for chiral assembly is that the particles or structures are intrinsically chiral or rendered so with adsorbed surface molecules and templates that create chirality (usually helical structures) or by lithographic methods (6-8). Chiral superstructures, especially those made from plasmonic nanoparticles, have distinctive optical properties such as circular dichroism (CD) under circularly-polarized light excitation (9-14), which have the potential for developing electric and optical sensors and devices (15-20). Templated assembly and lithography have been used to create chiral superstructures for sensing external stimuli through changes in CD spectra (21, 22). For example, DNA-templated assembly can transfer the helical configuration of DNA templates to many nanostructures (23-26) and be used to monitor changes in temperature and chemical binding (27-31).

Controlling the collective orientation of these chiral structures in either solution or solid matrices remains challenging for optimizing chiroptical performance. Besides, the existing strategies such as templated assemblies and chiral superlattice formation only work for materials of narrow length scales and specific chemical compositions or shapes (32-34). Unlocking the potential for designing miniature chiroptical devices and understanding light-matter interactions involving distinct physical principles would benefit from a general approach for assembling achiral materials of diverse sizes, shapes, and chemical compositions into chiral superstructures with actively tunable chiroptical responses (35-37).

Here, we report the rapid and reversible assembly of materials of varying compositions and length scales from small molecules to nano- and microstructures into chiral structures and active tuning of the structural handedness, collective orientation, and chiroptical properties using the magnetic field of a permanent magnet. Our analytical model demonstrates the presence of a quadrupole field chirality in the gradient magnetic field of the magnet. Assembling nanorods in such a magnetic field led to the formation of chiral superstructures, with their handedness and chiroptical properties being determined by magnet position and orientation. The structural chirality could be transferred to organic molecules and inorganic compounds by doping into or coating onto the host magnetic building blocks, demonstrating a general approach to chiral superstructures.

The quadrupole field chirality of permanent magnets

5

10

15

20

25

30

35

40

45

We consider the magnetic field and field distribution of a cube-shaped permanent magnet (**fig. S1**), with the north pole of the magnet pointing upward in **fig. S1A**. The calculated azimuth of the local magnetic field (mapped in **Fig. 1A**) undergoes gradual changes in the field direction in each quadrant. A differential magnetic field was calculated by subtracting magnetic field vectors in two chosen y-z cross sections (**fig. S2**). In **Fig. 1B**, the resulting local field rotation is indicated by the black arrows, and the magnitude is color-mapped, with the rotation angle ($\Delta\omega$) being defined as the differences between the azimuth of the magnetic fields in the two cross sections. The differential field forms a quadrupole, with two left-handed (positive $\Delta\omega$ in red domains) and right-handed (negative $\Delta\omega$ in blue domains) magnetic field domains. **Fig. S3** further delineates the rotation of local fields along a chosen pathway, demonstrating the helical magnetic field distribution.

We developed an analytical model to understand the assembly of magnetic nanorods in such a chiral field (see Supplementary Information for details) that could predict magnetic nanorod alignment along the local field to form chiral superstructures (**Figs. 1C** and **fig. S4**). For small magnetic nanorods $(107.6 \pm 5.2 \text{ nm} \text{ in length}, 13.0 \pm 1.7 \text{ nm} \text{ in diameter})$, there were no obvious

CD signals in rod dispersion without a magnetic field or in a magnetic field along the x-axis (Bx), but changing the field direction from the x-axis to y- and z-axis created CD responses (Fig. 1, D and E). We observed positive and negative CD peaks of similar intensity for y- (By) and z-field (Bz), respectively, which suggested chiral superstructures with opposite handedness. The CD responses were then measured in an aqueous solution of glycerol (n=1.475) with an increasing volume ratio from 0% to 100%. The increase in effective refractive index (n) of the solution induced consistent CD intensity decrease under the same magnetic fields (fig. S5). The nanorods' CD signal weakens but does not disappear as the solution refractive index approaches that of the SiO₂ layers ($n=1.475\pm0.005$) (38). This refractive index matching experiment demonstrates that both the scattering and absorption of the nanorods contribute to the overall CD responses. We calculated an optical anisotropic factor (g-factor) of ~ 0.01 at 400 nm (fig. S6). To verify the formation of chiral superstructures, Cyanine 3-doped Fe₃O₄@SiO₂ nanorods (322.2±16.5 nm in length, 70.2 ± 4.7 nm in diameter, and 50.3 ± 1.5 nm in silica thickness) were used as magnetic building blocks (39, 40) and fixed in a polymer by photocuring under a uniform magnetic field. Linear chains were formed because of magnetic dipole-dipole interactions and were parallel to the uniform field with a standard deviation of 0.36 degrees to minimize the demagnetizing fields (figs. S7 and S8) (41). If a gradient field of a permanent magnet (cube shape, 12 mm in edge length) was used (fig. S9), the chain alignment within one y-z plane and chain rotation between different y-z planes were determined by the local magnetic fields and field rotation, respectively (figs. S10 and S11). Thus, the chiral superstructures made of large nanorods show similar CD responses to magnetic fields (fig. S12). Besides, we characterized the chain alignment in ten sequential y-z layers from x=1 mm to 10 mm and in five layers along the y-axis using optical and electron microscopy, confirming the chain rotation into chiral superstructures as driven by the quadrupole chiral field (figs. S13-S17).

Magnetic assembly and active tuning of plasmonic chiral superstructures

5

10

15

20

25

30

35

40

45

To systematically study the CD dependence on magnetic fields over a wide spectral range, we introduced Fe₃O₄/Au hybrid nanorods as building blocks by taking advantage of the localized surface plasmon resonance (LSPR) of Au nanorods and the magnetic responses of Fe₃O₄ nanorods. The Au nanorods were synthesized using a space-confined growth method and had a length of 156.6 ± 15.2 nm and a diameter of 48.9 ± 4.7 nm (42, 43). As shown in **fig. S18A**, Fe₃O₄@SiO₂ nanorods were introduced (107.6 \pm 5.2 nm in length, 13.0 \pm 1.7 nm in diameter, 5.0 \pm 0.5 nm in silica thickness) as initial templates, followed by Au seed attachment (~ 2.0 nm in diameter). During polymer coating, the SiO₂ shells were etched away, and defined gaps were formed between the Fe₃O₄ nanorods and polymer shells. Seeded growth was performed inside the gaps to prepare the hybrid nanorods, which comprise one Au nanorod and one Fe₃O₄ nanorod in a parallel configuration, as shown in the transmission electron microscopy (TEM) images (Fig. 2A) and elemental mapping in fig. S19. Due to the confinement of the polymer shells, radial growth was limited, and preferable longitudinal growth produced the Au nanorods. This growth mode allows easy tuning of the nanorod length (fig. S18, B to E) and shifts the LSPR of the Au nanorods from 560 nm to 880 nm (fig. S18F). The parallel alignment of the hybrid nanorods allowed the Au nanorods to assemble into chiral superstructures under a chiral magnetic field and produce CD responses (fig. S20, A and B). Switching the magnet dipole did not alter the CD profile, but changing the magnet position to the opposite side of the sample produced a CD spectrum with an opposite sign (fig. S20C). Applying two identical magnets in their attraction configuration generated a parallel magnetic field with a reduced field gradient between the two magnets and

reduced the CD signals (**fig. S20, D** and **E**). The disappearance of CD signals confirmed that linear superstructures assembled in a uniform magnetic field could not produce CD signals in our experimental conditions. We also fixed the hybrid nanorods under the absence and presence of uniform and chiral magnetic fields using a photocuring polymerization method, which produced random, linear, and chiral structures, respectively. While films containing random and linear structures were not optically active, the film with chiral superstructures had CD signals. None of the three structures showed evident responses to a magnet once fixed in polymer films (**fig. S21**). These experiments suggested that the observed CD responses in a single permanent magnet were not induced by extrinsic chirality, a CD property of achiral superstructures (44), or by magnetic circular dichroism (45).

5

10

15

20

25

30

35

40

45

We measured the CD spectra of Au nanorods while changing the position of the magnet vertically (Fig. 2B and figure S22, A and B). The CD signal declined gradually after the magnet was moved from -1.25 cm to 0 cm along the z-axis (vertical direction) (fig. S22, C and D), and the spectra changed the sign across 0 cm (Fig. 2C) in response to the field chirality changes shown in fig. S22, E and F. The dependence of CD signals on magnet position was similar when the magnet dipole was along the z-axis (fig. S23). Changing the samples' position relative to the magnet was equivalent but induced CD intensity decrease if the sample-magnet separation increased up to 3.0 cm along the x-axis (fig. S24). The CD spectra of Au nanorods were then measured by decreasing field strength from 31.2 to 25.1, 18.3, 12.9, and 5.5 mT, which corresponded to the magnet being 2.3, 2.5, 3, 4, and 5 cm away from the nanorod dispersion. We observed a consistent decrease in CD intensity for Au nanorods with different LSPR positions and for left- and right-handed chiral superstructures (Fig. 2, D and E, and fig. S25), which corresponded to the decrease in field rotation when the magnet departed the sample (Fig. 2F). Detailed field analysis in Fig. 2, G to J indicated that the rotation angle $(\Delta\omega)$ decreased consistently in the four chiral domains for increasing magnet-sample separation. The sample in the first quadrant was in a left-handed field in the By field (Fig. 2, G and H), which caused the negative signals in CD spectra. In the Bz field, the chiral field in the first quadrant produced positive CD signals (Fig. 2, I and J). The extinction and CD peak intensity of the hybrid nanorods were linearly proportional to Au concentration at fixed magnet and sample positions (fig. S26), which was consistent with Beer's law and molar ellipticity in CD. To verify the chiroptical properties, we modeled the chiral superstructures and calculated their CD spectra using a finite element method. The simulated spectra in figs. S27 demonstrated CD responses of Au nanorods with large separations. Considering the lack of positional order of nanorods in experiments, complex models were further developed to resolve the structures in figs. S15 and S17. These models contain nanorods with random positions but constant rotation in different planes (fig. S28), resembling the nanorod alignment in different cross-sections in the SEM images. The simulated CD spectra show rotation angle-dependent CD responses, which explains the decrease of CD intensity with the rotation angles of magnetic fields. Similar dependence is also observed in nanorods of increasing aspect ratios, and the continuous redshift of CD peaks in fig. S29 is qualitatively consistent with the measured CD spectra in fig. 25.

Changing the directions of the magnetic field produced more complex CD responses. We considered the rotation of the magnet within the x-y and y-z planes to explain the involved mechanisms (**Fig. 3A**). The alignment of the magnetic dipole of the magnet relative to the axes was defined by the azimuth angle Θ . The CD spectra showed intensity changes when Θ increased to 180° in the x-y plane (**Fig. 3B**), which increased to a saturated value and decreased again (**fig. S30**). Given the magnet was rotated in the x-y plane (**fig. S31**), the local magnetic fields and the field distribution were analyzed for different Θ values. The schemes in **fig. S31** illustrate the magnet's constant position and varying orientation.

Because the incident light was along the x-axis, the magnetic fields within the measured domains in the y-z and x-z planes were further plotted in Figs. 3C and 3D, respectively. We observed only slight changes in field direction and field distribution within the y-z plane for different magnet orientations (Fig. 3C). In the x-y planes, however, the field distribution exhibited dramatic changes when Θ increased to 90°, which led to excitation of longitudinal mode with gradually increased strength (Fig. 3D). For incident light along x-axis, the plasmonic excitation of Au nanorods was determined and could be predicted by the nanorod alignment, light incidence, and light polarization (46). Due to the changes in magnetic field direction and distribution in fig. S32, there was an associated change in the LSPR excitation of the Au nanorods when Θ increased to 90° . At 0° , the field was nearly parallel to the x-axis, and the resulting parallel alignment of nanorods to the incident light suppressed the longitudinal mode. At 90°, the magnetic field being nearly parallel to the z-axis led to the excitation of the longitudinal mode. We could predict the longitudinal extinction of the Au nanorods through the equation $\sin^2(\phi)$ where ϕ is the angle between the local field direction and the light incident direction. Fig. 3E showed a symmetric trend, with maximum extinction between 60° and 120°. Comparison of the predicted longitudinal extinction to the CD intensity measured at different Θ (Fig. 3F) suggested that CD intensity would depend on the magnet azimuth angle and that the CD responses of the assembled superstructures would be determined by the longitudinal extinction changes when the magnet azimuth increased within the x-y plane.

Changing the magnet azimuth in the y-z plane led to a different CD response, with a mechanism associated with field chirality changes. The measured CD spectra are shown in **fig. S33**, and the CD peaks at 545 nm and 698 nm simultaneously switch their signs at about 20° and 110° during the measurement (color map in **Fig. 4A**), which suggested handedness changes of the assembled superstructures. To verify this hypothesis, we used the analytical model to directly map the local field rotation direction, chirality, and handedness (**fig. S2**). At Θ =0°, the sample was 2 cm away from the magnet center, with an upward offset of 0.5 cm, which led to an azimuth of ~14° relative to the magnet center (**fig. S34**). Understanding the CD spectrum at Θ =0° required access to field properties at this specific sample location in the y-z plane.

The CD changes In response to magnet rotation were studied by analyzing the local field properties in different azimuth angles. In **Fig. 4B**, the plots of field distribution and field chirality within the y-z plane showed a similar quadrupole field chirality. The normalized field vectors at x = -0.2 cm and x = -0.8 cm were superimposed in **Fig. 4B** to illustrate local field rotation. The field rotation angles along a trajectory highlighted in **fig. S34C** are shown in **Fig. 4C**, which corresponds to the field changes during experimental measurement. The rotation angle ($\Delta\omega$) was initially positive but changed its sign at $\Theta=15^{\circ}$ and 105° , consistent with the experimental chirality transition angles plotted in **Fig. 4D**. The Pearson correlation coefficients between the field rotation angles and CD intensity at 698 nm and 545 nm are -0.989 and 0.987, respectively (**fig. S35**). The strong negative and positive correlation indicates that the field chirality changes could explain the dependence of the superstructure handedness and CD spectra on magnet rotation in the y-z plane.

Optical rotatory dispersion

5

10

15

20

25

30

35

40

45

We also studied the optical rotatory dispersion (ORD), which measures the polarization rotation of a linearly polarized light. Left- and right-handed circularly polarized light interacts differently with chiral structures and travels at a different speed inside them. Because linearly polarized light comprises two circularly polarized light beams with the same magnitude but opposite handedness,

these two highly correlated beams will develop a phase difference, leading to the polarization rotation of the incident beam (**Fig. 4E**). The ORD effect was tested by applying an analyzer to the incident beam and observing the color changes. Only light of a specific wavelength can pass through the analyzer at a polarization angle (α) if the material is optically active. Experimentally, α is defined as the angle between the analyzer polarization direction and the horizontal baseline, and the polarization of the polarizer is fixed along the vertical direction.

5

10

15

20

25

30

35

40

Digital images of a nanorod dispersion are shown in **Fig. 4F** before (left image) and after (right image) application of a z-directional magnetic field at α =3°. The original dispersion appeared dark without noticeable colors because only minimal light could transmit through the analyzer. Under a z-directional magnetic field, the top domain turned yellow and the bottom red, demonstrating the formation of chiral superstructures with opposite handedness in these two domains, consistent with the predicted field chirality in the first and fourth quadrants of the magnet. This ORD effect was determined by superstructure handedness and the angle α . Under a z-directional magnetic field, similar two-color domains were observed when α increased from -30° to 30° (**Fig. 4G**), with redorange-yellow-green changes in the top domain and opposite color changes in the bottom domain. Changing the magnetic field to the y-axis led to color switching between the two domains, corresponding to a field chirality transition. Nanorod dispersion under the absence and presence of the x-directional magnetic field only exhibited contrast changes at different α because of the negligible CD responses at these two conditions.

Generalizing the all-scale chiral assembly: from nanostructures to molecules

The chirality formed by nanoscale magnetic assembly could be transferred to organic molecules, polymers, oxides, and semiconductors. These guest materials were introduced to the magnetic nanorods through surface coating and doping methods, which have the advantages of wide material accessibility and easy further processing. Starting with Fe₃O₄@SiO₂ nanorods with a length of 107.6 ± 5.2 nm, a diameter of 13.0 ± 1.7 nm, and silica thickness of 5.0 ± 0.5 nm, we coated their surface with Cu₂O nanoparticles and resorcinol-formaldehyde (RF), with the latter being converted into MnO₂ by reacting with kMnO₄ (47-49). The resulting Fe₃O₄@SiO₂@MnO₂ nanorods (Fig. 5A) underwent oxidation-induced volume expansion and created nanogaps between porous MnO₂ nanoshells and Fe₃O₄@SiO₂ cores. The extinction spectra of these samples in Fig. 5B showed broad extinction of Fe₃O₄@SiO₂ and Fe₃O₄@SiO₂@Cu₂O nanorods and extinction peaks of Fe₃O₄@SiO₂@RF and Fe₃O₄@SiO₂@MnO₂ nanorods. These four samples showed evident CD activities under magnetic fields that can also be tuned by changing the field directions (Fig. 5C). The CD peak positions being near their extinction peak positions indicates that the chirality in the superstructures transferred from the host nanorods to the guest molecules. In addition, changing the field direction from the y-axis to the z-axis changed the chiral superstructures from left-handed to right-handed symmetry.

Transfer of chirality to small molecules was demonstrated by doping organic dyes into RF polymeric shells through electrostatic interactions. **Fig. S36A** shows a typical TEM image of the Fe₃O₄@SiO₂@RF nanorods with 100-nm RF shells that carry negative charges after a condensation reaction. Three dyes, including methylene blue, methylene green, and neutral red, are chosen with their molecular structures given in **fig. S36B**. These dyes develop positive charges after dissociation of chloride anions in water and can be doped into porous RF shells by mixing with the nanorods at room temperature. **Fig. 5D** show that the dyed solutions appeared blue, green,

and red after removing the excess molecules, with extinction spectra exhibiting distinct peaks after successful doping.

Using the green dye-doped nanorods as an example, we confirmed their CD responses under different field directions (**fig. S36C**), with negligible CD signals under no and x-directional magnets and opposite CD peaks in y- and z-directional magnetic fields. The CD spectra of nanorods doped with all three dyes (**Fig. 5E**) showed peaks at their characteristic wavelengths. The observation is consistent with that of plasmonic nanorods and demonstrated the formation of chiral superstructures and the successful transfer of chirality from the nanoscale to molecular levels. The g-factor calculated in **Fig. 5F** has a maximum of ~0.003 for methylene blue-doped nanorods, a value comparable to that of classic chiral molecules and magnetically assembled chiral superstructures of inorganic molecules, polymers, and semiconductors (**figs. S37** and **S38**). We further demonstrated that the magnetic assembly strategy could be extended to the assembly of fluorophores for generating circularly polarized luminescence. When Europium-doped NaYF₄ nanorods were decorated with Fe₃O₄ nanoparticles, the fluorescent nanorods could be assembled into chiral superstructures and exhibited circularly polarized luminescence (**fig. S39**).

Discussion

5

10

15

20

25

30

35

40

The consistent rotation of the local field vectors of the cubic permanent magnet forms the quadrupole field chirality with alternating left-handed and right-handed magnetic fields in the four quadrants. Such chiral magnetic fields induce the assembly of magnetic nanorods into chiral superstructures, with handedness and chirality determined by the local features of the magnetic fields. This strategy allows remote, reversible, and instantaneous assembly of chiral superstructures from nanostructures of various chemical compounds (plasmonic materials, polymers, oxides, metals, semiconductors, fluorescent nanostructures, and molecular moieties) and active tuning of their CD responses in a broad range of spectra and circularly polarized luminescence, as long as they can be properly bound to the magnetic nanorods. Fixing the chirality of these chemical compounds at all scales is possible by embedding the formed superstructures in polymer substrates, which could be realized by applying an external magnetic field during polymerization. This simple strategy makes the chiral superstructures nonvolatile without external magnetic fields and highly accessible for portable chiroptical devices.

References and Notes

- 1. G. Singh, H. Chan, A. Baskin, E. Gelman, N. Repnin, P. Král, R. Klajn, Self-assembly of magnetite nanocubes into helical superstructures. *Science* **345**, 1149-1153 (2014).
- 2. X. Lan, X. Lu, C. Shen, Y. Ke, W. Ni, Q. Wang, Au nanorod helical superstructures with designed chirality. *Journal of the American Chemical Society* **137**, 457-462 (2015).
- 3. W. Ma, L. Xu, A. F. de Moura, X. Wu, H. Kuang, C. Xu, N. A. Kotov, Chiral inorganic nanostructures. *Chemical Reviews* **117**, 8041-8093 (2017).
- 4. J. Lv, X. Gao, B. Han, Y. Zhu, K. Hou, Z. Tang, Self-assembled inorganic chiral superstructures. *Nature Reviews Chemistry* **6**, 125-145 (2022).
- 5. M. Hentschel, M. Schäferling, X. Duan, H. Giessen, N. Liu, Chiral plasmonics. *Science advances* **3**, e1602735 (2017).
- 6. C. Zhou, X. Duan, N. Liu, DNA-nanotechnology-enabled chiral plasmonics: from static to dynamic. *Accounts of Chemical Research* **50**, 2906-2914 (2017).

7. R. Schreiber, N. Luong, Z. Fan, A. Kuzyk, P. C. Nickels, T. Zhang, D. M. Smith, B. Yurke, W. Kuang, A. O. Govorov, Chiral plasmonic DNA nanostructures with switchable circular dichroism. *Nature communications* 4, 1-6 (2013).

5

10

15

25

30

35

40

- 8. D. Zerrouki, J. Baudry, D. Pine, P. Chaikin, J. Bibette, Chiral colloidal clusters. *Nature* **455**, 380-382 (2008).
- 9. L. Xu, X. Wang, W. Wang, M. Sun, W. J. Choi, J.-Y. Kim, C. Hao, S. Li, A. Qu, M. Lu, Enantiomer-dependent immunological response to chiral nanoparticles. *Nature* **601**, 366-373 (2022).
- 10. N. A. Kotov, L. M. Liz-Marzan, P. S. Weiss. (ACS Publications, 2021), vol. 15, pp. 12457-12460.
- 11. K.-J. Jeong, D. K. Lee, V. T. Tran, C. Wang, J. Lv, J. Park, Z. Tang, J. Lee, Helical magnetic field-induced real-time plasmonic chirality modulation. *ACS nano* **14**, 7152-7160 (2020).
- 12. H.-E. Lee, H.-Y. Ahn, J. Mun, Y. Y. Lee, M. Kim, N. H. Cho, K. Chang, W. S. Kim, J. Rho, K. T. Nam, Amino-acid-and peptide-directed synthesis of chiral plasmonic gold nanoparticles. *Nature* **556**, 360-365 (2018).
- 13. W. Jiang, Z.-b. Qu, P. Kumar, D. Vecchio, Y. Wang, Y. Ma, J. H. Bahng, K. Bernardino, W. R. Gomes, F. M. Colombari, Emergence of complexity in hierarchically organized chiral particles. *Science* **368**, 642-648 (2020).
- 20 14. G. González-Rubio, J. Mosquera, V. Kumar, A. Pedrazo-Tardajos, P. Llombart, D. M. Solís, I. Lobato, E. G. Noya, A. Guerrero-Martínez, J. M. Taboada, Micelle-directed chiral seeded growth on anisotropic gold nanocrystals. *Science* **368**, 1472-1477 (2020).
 - 15. L. Ohnoutek, J.-Y. Kim, J. Lu, B. J. Olohan, D. M. Răsădean, G. Dan Pantoş, N. A. Kotov, V. K. Valev, Third-harmonic Mie scattering from semiconductor nanohelices. *Nature Photonics* **16**, 126-133 (2022).
 - 16. C. Hao, L. Xu, H. Kuang, C. Xu, Artificial chiral probes and bioapplications. *Advanced Materials* **32**, 1802075 (2020).
 - 17. F. Neubrech, M. Hentschel, N. Liu, Reconfigurable plasmonic chirality: fundamentals and applications. *Advanced Materials* **32**, 1905640 (2020).
 - 18. Y. Y. Lee, R. M. Kim, S. W. Im, M. Balamurugan, K. T. Nam, Plasmonic metamaterials for chiral sensing applications. *Nanoscale* **12**, 58-66 (2020).
 - 19. Z. Li, Q. Fan, Y. Yin, Colloidal self-assembly approaches to smart nanostructured materials. *Chemical Reviews* **122**, 4976-5067 (2021).
 - 20. N. J. Greenfield, Using circular dichroism spectra to estimate protein secondary structure. *Nature protocols* **1**, 2876-2890 (2006).
 - 21. B. Shen, V. Linko, K. Tapio, S. Pikker, T. Lemma, A. Gopinath, K. V. Gothelf, M. A. Kostiainen, J. J. Toppari, Plasmonic nanostructures through DNA-assisted lithography. *Science advances* 4, eaap8978 (2018).
 - 22. B. Frank, X. Yin, M. Schäferling, J. Zhao, S. M. Hein, P. V. Braun, H. Giessen, Largearea 3D chiral plasmonic structures. *ACS nano* 7, 6321-6329 (2013).
 - 23. A. Kuzyk, R. Schreiber, Z. Fan, G. Pardatscher, E.-M. Roller, A. Högele, F. C. Simmel, A. O. Govorov, T. Liedl, DNA-based self-assembly of chiral plasmonic nanostructures with tailored optical response. *Nature* **483**, 311-314 (2012).
 - 24. D. Winogradoff, P. Y. Li, H. Joshi, L. Quednau, C. Maffeo, A. Aksimentiev, Chiral systems made from DNA. *Advanced Science* **8**, 2003113 (2021).
 - 25. K. Martens, F. Binkowski, L. Nguyen, L. Hu, A. O. Govorov, S. Burger, T. Liedl, Longand short-ranged chiral interactions in DNA-assembled plasmonic chains. *Nature communications* **12**, 1-6 (2021).

- Y. Chen, W. Du, Q. Zhang, O. Ávalos-Ovando, J. Wu, Q.-H. Xu, N. Liu, H. Okamoto, A. O. Govorov, Q. Xiong, Multidimensional nanoscopic chiroptics. *Nature Reviews Physics* 4, 113-124 (2022).
- 27. P. Zhan, M. J. Urban, S. Both, X. Duan, A. Kuzyk, T. Weiss, N. Liu, DNA-assembled nanoarchitectures with multiple components in regulated and coordinated motion. *Science advances* 5, eaax6023 (2019).
- 28. L. Xin, C. Zhou, X. Duan, N. Liu, A rotary plasmonic nanoclock. *Nature communications* **10**, 1-8 (2019).

10

15

20

25

30

35

- 29. S. Li, L. Xu, W. Ma, X. Wu, M. Sun, H. Kuang, L. Wang, N. A. Kotov, C. Xu, Dual-mode ultrasensitive quantification of microRNA in living cells by chiroplasmonic nanopyramids self-assembled from gold and upconversion nanoparticles. *Journal of the American Chemical Society* **138**, 306-312 (2016).
- 30. A. Cecconello, L. V. Besteiro, A. O. Govorov, I. Willner, Chiroplasmonic DNA-based nanostructures. *Nature Reviews Materials* **2**, 1-19 (2017).
- 31. A. Kuzyk, M. J. Urban, A. Idili, F. Ricci, N. Liu, Selective control of reconfigurable chiral plasmonic metamolecules. *Science Advances* **3**, e1602803 (2017).
 - 32. S. Zhou, J. Li, J. Lu, H. Liu, J.-Y. Kim, A. Kim, L. Yao, C. Liu, C. Qian, Z. D. Hood, Chiral assemblies of pinwheel superlattices on substrates. *Nature*, 1-7 (2022).
 - 33. Z. Cheng, M. R. Jones, Assembly of planar chiral superlattices from achiral building blocks. *Nature Communications* **13**, 4207 (2022).
 - 34. J. Lu, Y. Xue, K. Bernardino, N.-N. Zhang, W. R. Gomes, N. S. Ramesar, S. Liu, Z. Hu, T. Sun, A. F. de Moura, Enhanced optical asymmetry in supramolecular chiroplasmonic assemblies with long-range order. *Science* **371**, 1368-1374 (2021).
 - 35. G. M. Whitesides, B. Grzybowski, Self-assembly at all scales. *Science* **295**, 2418-2421 (2002).
 - 36. X. Lan, Q. Wang, Self-assembly of chiral plasmonic nanostructures. *Advanced Materials* **28**, 10499-10507 (2016).
 - 37. C. A. Silvera Batista, R. G. Larson, N. A. Kotov, Nonadditivity of nanoparticle interactions. *Science* **350**, 1242477 (2015).
- 38. B. N. Khlebtsov, V. A. Khanadeev, N. G. Khlebtsov, Determination of the size, concentration, and refractive index of silica nanoparticles from turbidity spectra. *Langmuir* **24**, 8964-8970 (2008).
 - 39. W. Xu, M. Wang, Z. Li, X. Wang, Y. Wang, M. Xing, Y. Yin, Chemical transformation of colloidal nanostructures with morphological preservation by surface-protection with capping ligands. *Nano Letters* **17**, 2713-2718 (2017).
 - 40. Z. Li, C. Qian, W. Xu, C. Zhu, Y. Yin, Coupling morphological and magnetic anisotropy for assembling tetragonal colloidal crystals. *Science advances* 7, eabh1289 (2021).
 - 41. M. Wang, Y. Yin, Magnetically responsive nanostructures with tunable optical properties. *Journal of the American Chemical Society* **138**, 6315-6323 (2016).
- 42. Z. Li, J. Zhang, J. Jin, F. Yang, R. Aleisa, Y. Yin, Creation and Reconstruction of Thermochromic Au Nanorods with Surface Concavity. *Journal of the American Chemical Society* **143**, 15791–15799 (2021).
 - 43. Z. Li, J. Jin, F. Yang, N. Song, Y. Yin, Coupling magnetic and plasmonic anisotropy in hybrid nanorods for mechanochromic responses. *Nature communications* **11**, 1-11 (2020).
 - 44. E. Plum, V. Fedotov, N. Zheludev, Optical activity in extrinsically chiral metamaterial. *Applied physics letters* **93**, 191911 (2008).

- 45. B. Han, X. Gao, J. Lv, Z. Tang, Magnetic circular dichroism in nanomaterials: New opportunity in understanding and modulation of excitonic and plasmonic resonances. *Advanced Materials* **32**, 1801491 (2020).
- 46. M. Wang, C. Gao, L. He, Q. Lu, J. Zhang, C. Tang, S. Zorba, Y. Yin, Magnetic tuning of plasmonic excitation of gold nanorods. *Journal of the American Chemical Society* **135**, 15302-15305 (2013).
- 47. C. Liu, H. Dong, N. Wu, Y. Cao, X. Zhang, Plasmonic resonance energy transfer enhanced photodynamic therapy with Au@ SiO2@ Cu2O/perfluorohexane nanocomposites. *ACS applied materials & interfaces* **10**, 6991-7002 (2018).

10

15

20

25

- 48. S. Zhou, Y. Bai, W. Xu, J. Feng, X. Wang, Z. Li, Y. Yin, Formation of resorcinol-formaldehyde hollow nanoshells through a dissolution–regrowth process. *Nanoscale* **12**, 15460-15465 (2020).
 - 49. Y. Bai, X. Yao, X. Wang, Y. Yin, Surface-Initiated Redox Route to Hollow MnO2 Nanostructures. *ChemNanoMat* **6**, 1186-1190 (2020).
- 50. The programming code to model magnetic fields and datasets used to analyze the field chirality are available online at Zenodo via https://zenodo.org/record/7686903#.ZA3s45HMK5d
 - 51. X. Xue, E. P. Furlani, Analysis of the dynamics of magnetic core—shell nanoparticles and selfassembly of crystalline superstructures in gradient fields. The Journal of Physical Chemistry C 119, 5714-5726 (2015).
 - 52. E. P. Furlani, Permanent magnet and electromechanical devices: materials, analysis, and applications. (Academic press, 2001).
 - 53. H. Zhang, G. Ahmadi, F.-G. Fan, J. B. McLaughlin, Ellipsoidal particles transport and deposition in turbulent channel flows. Int. J. Multiphase Flow 27, 971-1009 (2001).
 - 54. K. Li, H. Ma, Deposition dynamics of rod-shaped colloids during transport in porous media under favorable conditions. Langmuir 34, 2967-2980 (2018).
 - 55. H. Brenner, The Stokes resistance of an arbitrary particle—II: An extension. Chem. Eng. Sci. 19, 599-629 (1964).
 - 56. G. B. Jeffery, The motion of ellipsoidal particles immersed in a viscous fluid. Proceedings of the Royal Society of London. Series A, Containing papers of a mathematical and physical character 102, 161-179 (1922).
 - 57. F. Perrin, Mouvement brownien d'un ellipsoide-I. Dispersion diélectrique pour des molécules ellipsoidales. J. Phys. Radium. 5, 497-511 (1934).
- We thank the Central Facility for Advanced Microscopy and Microanalysis at UCR for help with 35 TEM analysis and Dr. Ung's group at University of Connecticut for assistance with measuring the circularly polarized luminescence. Funding: U.S. National Science Foundation CHE- 2203972 (YY); Authors contributions: Z. L. and Y. Y. conceived and planned this study. Z. L. and Q. F. developed the methodology for modeling and simulation. Z. L. developed the synthesis and characterization of nanoparticles. Z. L., Z. Y., and C. W. performed the CD measurements. Z. W. 40 contributed to the circularly polarized luminescence studies. All authors discussed and analyzed the results and contributed to the writing of this paper. Competing interests: Y.Y. and Z.L. are planning on a patent application related to this work filed by the University of California Riverside. The anthors declare that they have no other completing interests. Data and materials availability: All data needed to evaluate the conclusions in the paper are present in the paper or the 45 Supplementary Materials. The programming code to model magnetic fields and datasets used to chirality online analyze the field are available at Zenodo via https://zenodo.org/record/7686903#.ZA3s45HMK5d.

Supplementary Materials

Materials and Methods Supplementary Text Figs. S1 to S39

5 Table S1

References (51-57)

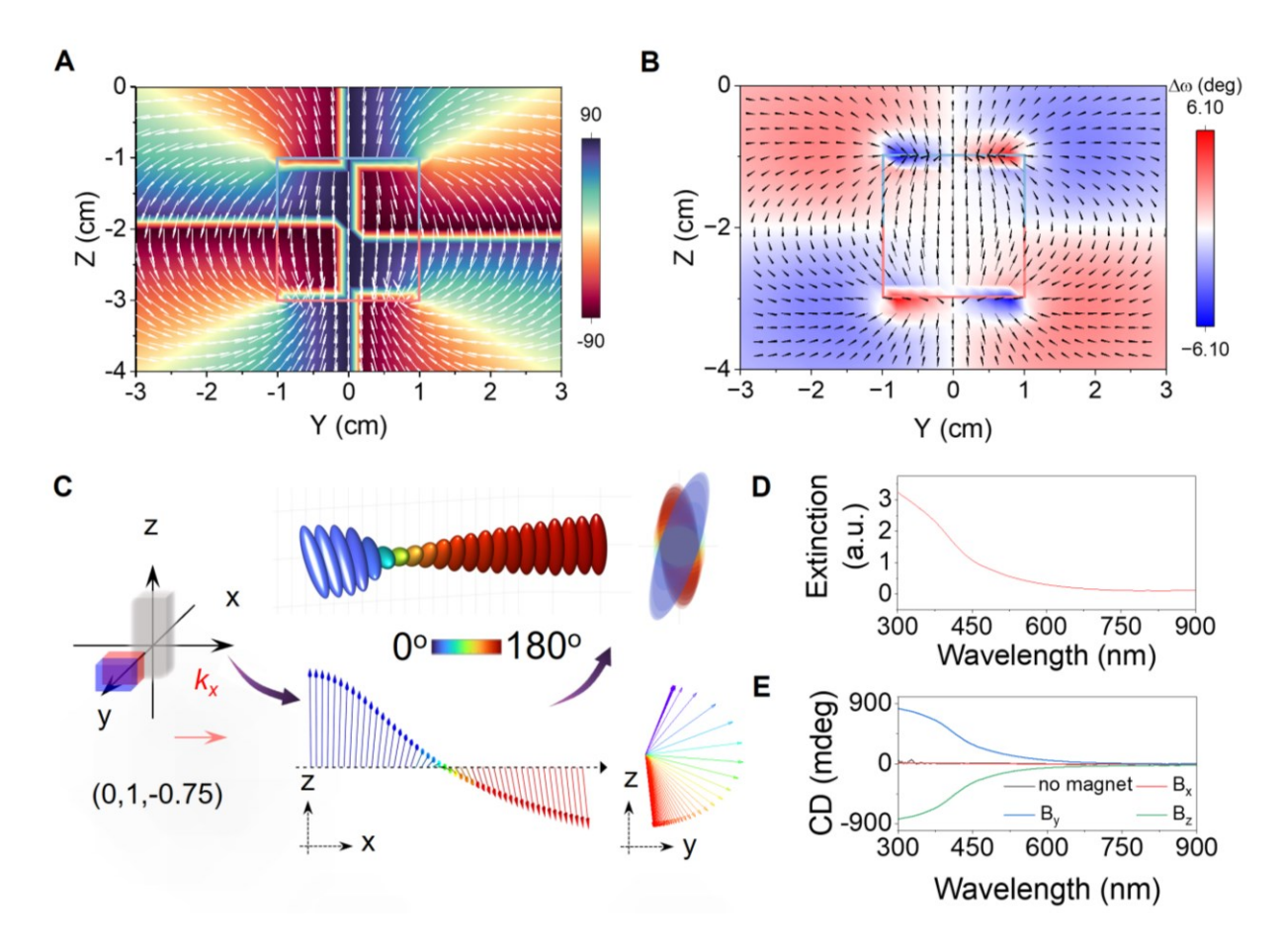


Fig. 1. The quadrupole field chirality of a permanent magnet. (A) Normalized magnetic field (white arrows) and field vector azimuth (color maps) of a permanent magnet (highlighted in the middle square) with a cubic shape and edge length of 2 cm. (B) The field rotating vectors (black arrows) and field angle changes (color map) of the magnetic field along the x-axis. Positive rotation angles ($\Delta\omega$) represent clockwise left-handed rotation of the magnetic field, and negative rotation angles represent counterclockwise right-handed field rotation. (C) Schematic illustration of the magnetic assembly during CD measurement and simulated helical superstructures assembled from magnetic nanorods under such a chiral magnetic field. (D) Extinction spectrum and (E) CD spectra of Fe₃O₄@SiO₂ nanorods under different magnetic fields.

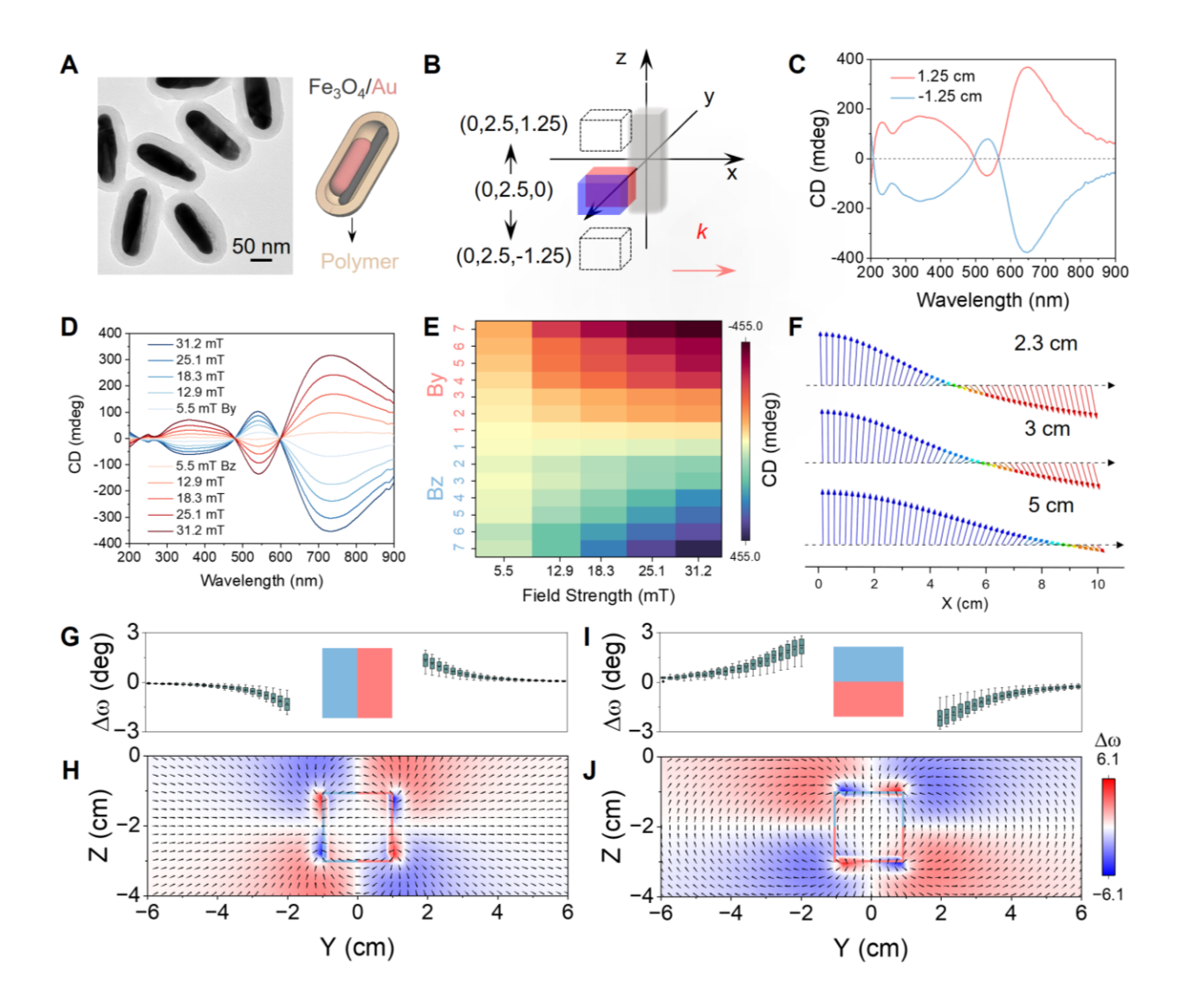


Figure 2. Magnetic assembly of Fe₃O₄/Au hybrid nanorods into chiral superstructures. (A) TEM image of the Fe₃O₄/Au hybrid nanorods wrapped within polymer shells. Inset: schematic structure of the Fe₃O₄/Au hybrid nanorods. (B) Schematic illustration of the magnet position during the CD measurement. (C) CD spectra of the hybrid nanorods measured by changing the magnet position. (D) CD spectra of the hybrid nanorods under magnetic fields with consistent direction and decreasing strength. (E) Dependence of CD intensity on the field strength and the rod aspect ratios. The magnetic fields are defined as By and Bz when the magnet dipole is parallel to y- and z-axis, respectively. (F) Simulated field distributions of the cubic magnet at given distances to the magnet surface. (G, I) Rotation angles of magnetic fields between two y-z cross sections, (-0.2, y, z) and (-0.8, y, z). The orientation of the magnet is shown in the inset in each plot. (H, J) The corresponding field rotation angles (color map) and the local magnetic field at the cross section (-0.2, y, z). The magnet has a horizontal magnetic dipole in (G, H) and a vertical magnetic dipole in (I, J). The field rotation is calculated by $\Delta\omega(y, z) = \omega(-0.8, y, z)-\omega(-0.2, y, z)$.

10

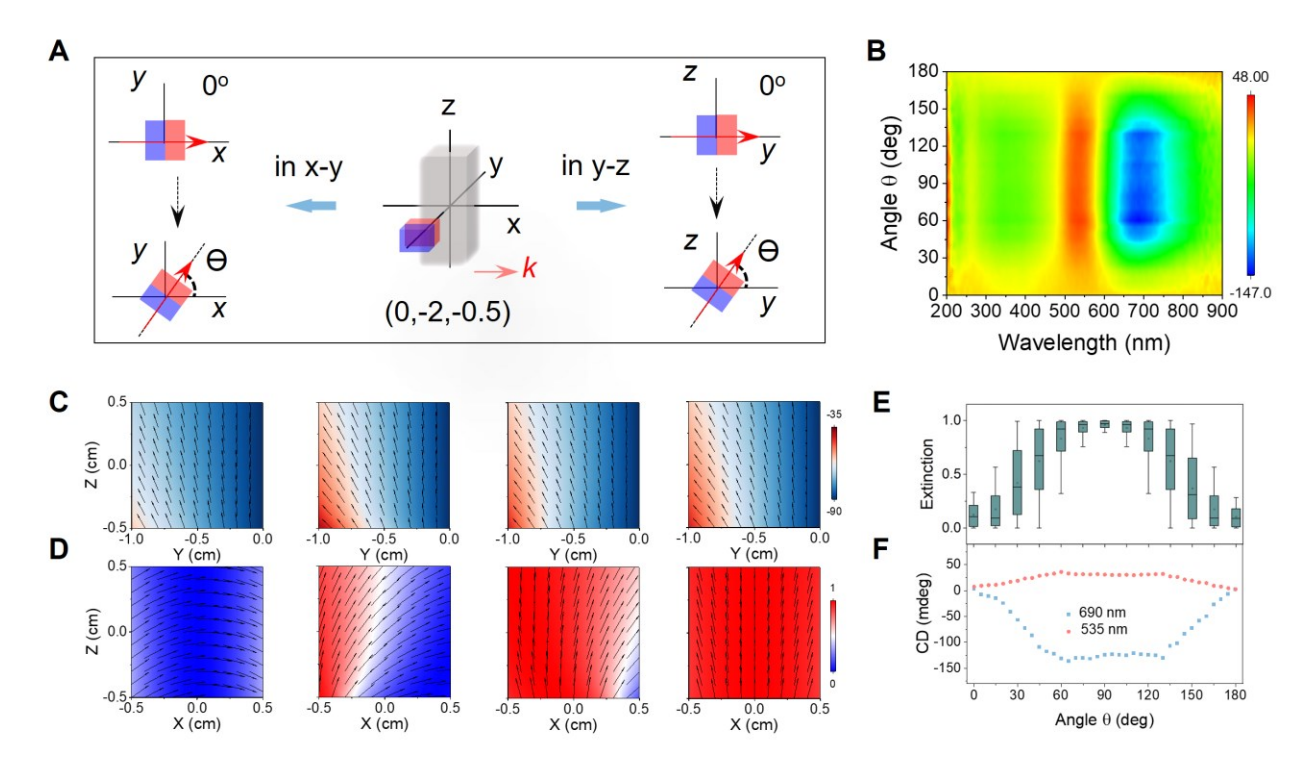


Figure 3. Tunable CD spectra of the assembled superstructures. (A) Schematic illustration of the azimuth changes of a cubic permanent magnet within the x-y and y-z plane during CD measurements. (B) CD spectra of the hybrid nanorods measured by changing the magnet azimuth in the x-y plane. The magnetic field of the cubic magnet in (C) y-z and (D) x-z planes. The azimuth of the magnet is 0° to 30° , 60° , and 90° from the left to the right panel. (E) Predicted longitudinal extinction of the nanorods based on the analytical solution. (F) Dependence of the CD intensity on magnetic field azimuth (Θ).

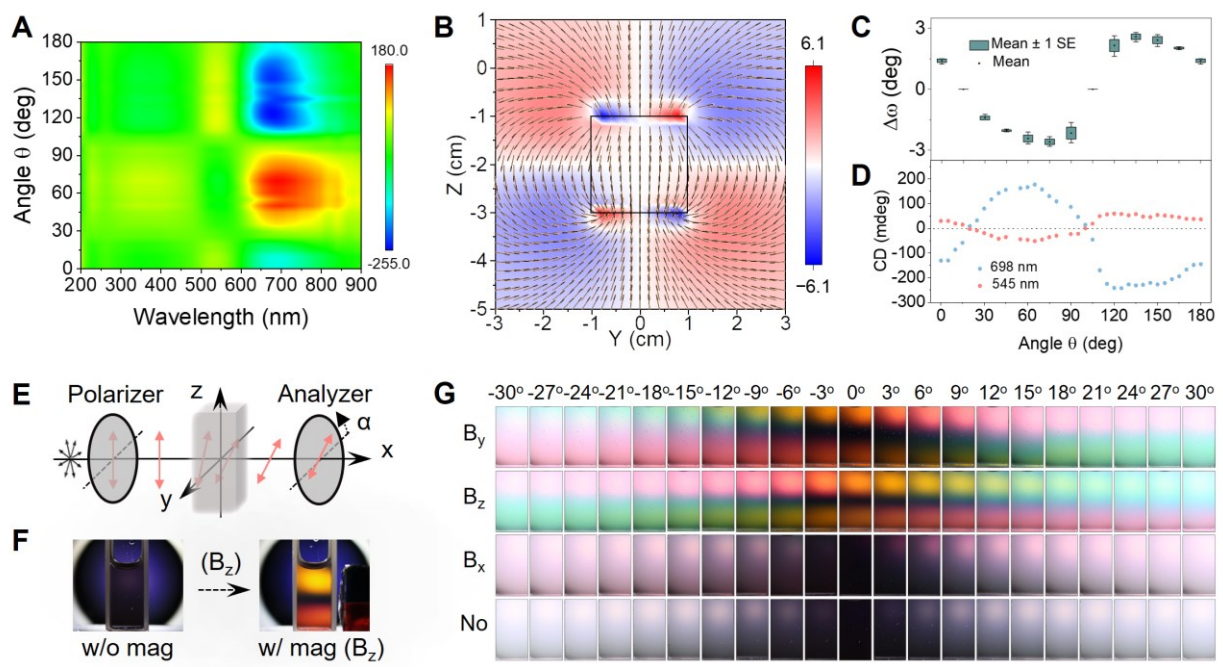


Figure 4. Tunable CD spectra and optical rotatory dispersion of the assembled superstructures. (A) CD spectra of the hybrid nanorods measured by changing the magnet azimuth in the y-z plane. (B) The magnetic field rotation (color map) and the normalized field vectors (arrows) of the cubic magnet. The magnetic field rotation is calculated by $\Delta\omega(y,z)=\omega(-0.8,y,z)-\omega(-0.2,y,z)$. The normalized magnetic field vectors in (-0.8, y, z) are presented by black arrows, and the field vectors in (-0.2, y, z) are presented by orange arrows. (C) Dependence of field rotation on the magnet field azimuth. (D) Dependence of the CD peak intensity on the magnet field azimuth. (E) Schematic illustration of the ORD measurement. The α is introduced as the angle between the polarization direction of the analyzer and the horizontal direction. (F) Digital images of a hybrid nanorod dispersion in a cuvette without (w/o mag) and with (w/ mag) a magnetic field. The α is 3°. (G) Digital pictures of the hybrid nanorod dispersion under different magnetic field conditions. The analyzer's polarization direction (α) was switched from -30° to 30° during the measurement.

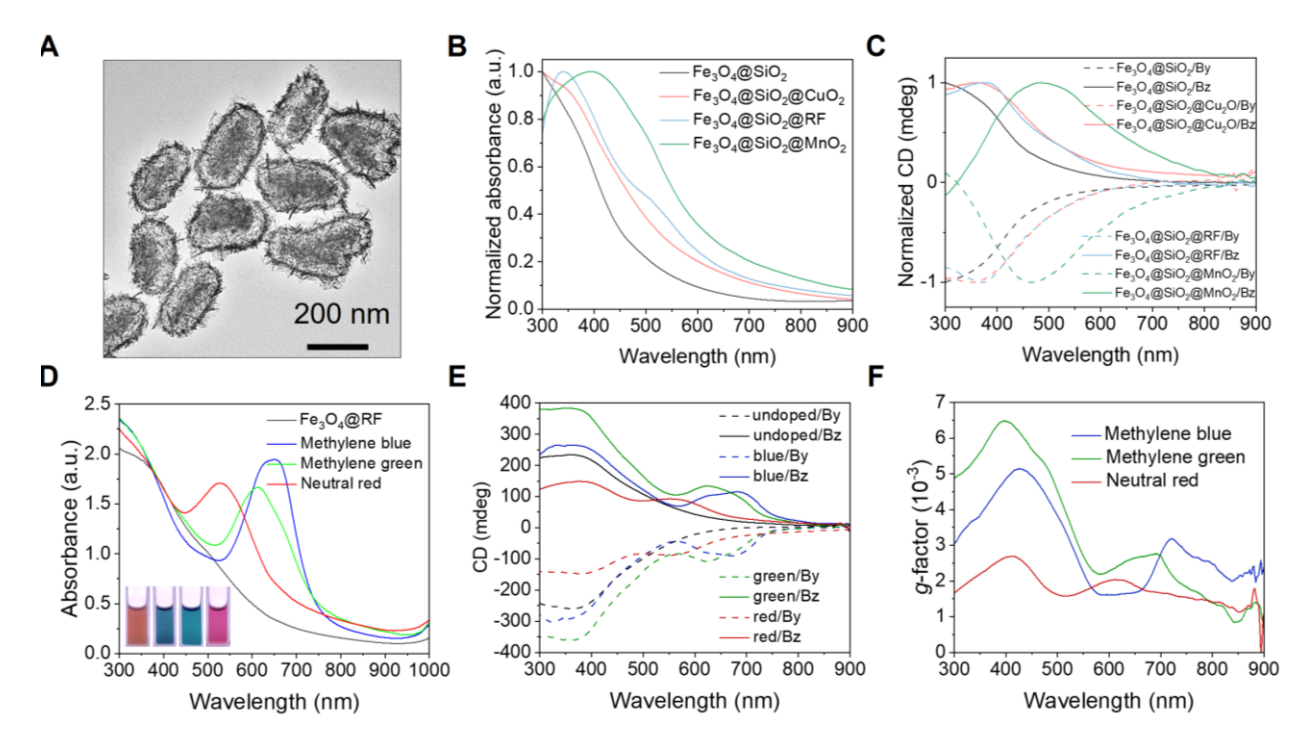


Figure 5. All-scale magnetic assembly of achiral molecules into chiral superstructures. (A) TEM image of the Fe₃O₄@SiO₂@MnO₂ core/shell nanorods. (B) Extinction spectra of core/shell Fe₃O₄@SiO₂ and Fe₃O₄@SiO₂@RF nanorods, Fe₃O₄@MnO₂ yolk/shell nanorods, and Fe₃O₄@SiO₂@Cu₂O core/satellite nanorods. (C) The corresponding CD spectra measured under y- and z-directional magnetic fields. (D) Extinction spectra of the Fe₃O₄@SiO₂@RF nanorods and nanorods doped with the three organic dyes. Insets from left to right: digital pictures of the nanorods before and after doping with methylene blue, methylene green, and neutral red. (E) CD spectra of the doped and undoped nanorods under y- and z-directional magnetic fields. (F) The g-factor of the doped nanorods under a z-directional magnetic field.